Synergy of Ni micro-alloying and thermomechanical processing in Al–Mg–Si–Cu–Zn–Fe–Mn alloys with enhanced bendability

Yuan, Bo; Li, Gaojie; Guo, Mingxing; Zhuang, Linzhong

DOI
10.1016/j.jmrt.2021.10.112

Publication date
2021

Document Version
Final published version

Published in
Journal of Materials Research and Technology

Available online at www.sciencedirect.com

jmr&t Journal of Materials Research and Technology

journal homepage: www.elsevier.com/locate/jmrt

Original Article

Synergy of Ni micro-alloying and thermomechanical processing in Al–Mg–Si–Cu–Zn–Fe–Mn alloys with enhanced bendability

Bo Yuan [a], *Gaojie Li* [c], *Mingxing Guo* [a,b,*], *Linzhong Zhuang* [a,b,**]

[a] *State Key Laboratory for Advanced Metals and Materials, University of Science and Technology Beijing, Beijing, 100083, China*

[b] *Beijing Laboratory of Metallic Materials and Processing for Modern Transportation, University of Science and Technology Beijing, Beijing 10083, China*

[c] *Department of Materials Science and Engineering, Delft University of Technology, 2628 CD Delft, the Netherlands*

ARTICLE INFO

Article history:
Received 23 September 2021
Accepted 25 October 2021
Available online 28 October 2021

Keywords:
Al–Mg–Si–Cu–Zn–Fe–Mn alloy
Micro-alloying
Synergy
Structure
Fe-rich phases
Mechanism

ABSTRACT

Synergy of Ni micro-alloying and thermomechanical processing on the phase distribution, formability and bendability of Al–Mg–Si–Cu–Zn–Fe–Mn alloys was systematically studied in this paper. With the addition of micro-alloying Ni, the Ni-containing Fe-rich phase can be formed, which not only serves as nucleation sites of Mg–Si precipitates (such as, Q phase) during the casting process, but also improves the uniform distribution level of Fe-rich phases after homogenization. The formability and bendability of Ni-containing alloy can be both improved to a certain level due to the positive effect of Ni micro-alloying. In comparison, if increasing the cold rolling deformation between hot rolling and annealing, the distribution of multi-scale Fe-rich phases can be significantly improved based on the synergy of Ni micro-alloying and thermomechanical processing. And finally, this improvement further results in the great improvements in the microstructure, texture, formability (average $\bar{r} = 0.688$, $\Delta r = -0.09$) and bendability of the alloy together. Based on the microstructure evolution, the synergy mechanism of Ni micro-alloying and thermomechanical processing is put forward in this paper.

1. Introduction

Al–Mg–Si(-Cu) alloys have been wildly used in automotive application due to their high specific strength, low density and good age hardening response. However, compared with steels, their lower strength, ductility, formability and bendability still need to be further improved in order to meet the demanding requirements [1–5]. Generally, the microstructure evolution

* Corresponding author.
** Corresponding author.
E-mail addresses: mingxingguo@skl.ustb.edu.cn (M. Guo), linzhongzhuang@yahoo.com (L. Zhuang).

https://doi.org/10.1016/j.jmrt.2021.10.112

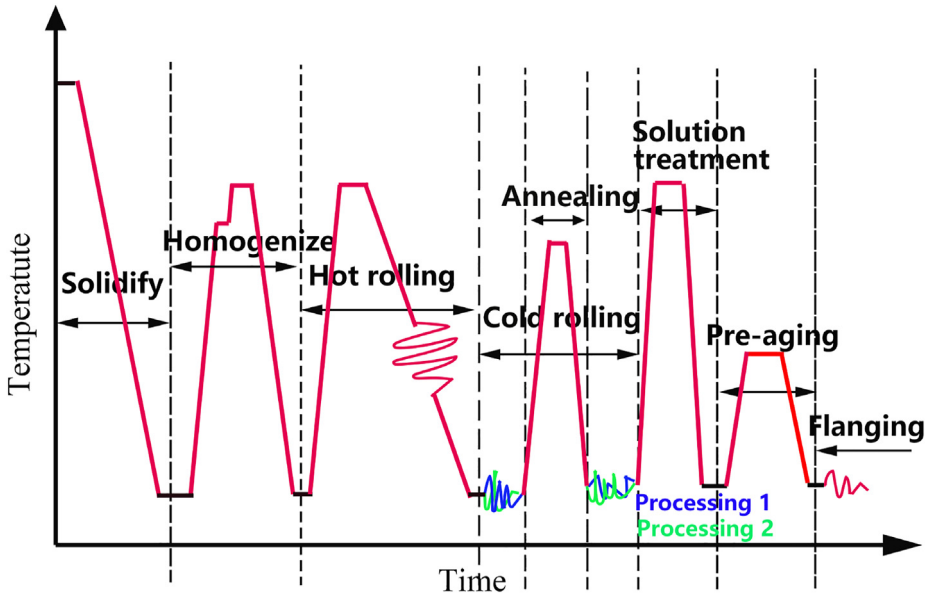

Fig. 1 – Schematic diagram of different thermomechanical processing routes used in the experimental alloys.

and mechanical properties of Al–Mg–Si alloys can be changed or improved after adding alloying elements, such as, Cu, Zn and so on [6–13]. For example, the addition of Cu (<0.2.wt %) can change precipitation sequence and the distribution of precipitates, and further enhance the peak aging strength. Unfortunately, the corrosion resistance of the alloys can be reduced due to the changed composition and distribution of precipitates [6,7]. Increasing Si content in Al–Mg–Si alloy can increase the strength as the Si content below the chemical composition ratio of Mg_2Si, but the corrosion resistance of the alloy can be slightly decreased [8]. Some results show that the addition of Zn can be used to improve the bake hardening response and the peak aging strength of Al–Mg–Si–Cu alloys [9–13], the Mg–Si–Cu–Zn solute clusters can be formed and acting as the nucleation sites of β″ phase, finally greatly improve the nucleation rate of β″ phase and bake hardening response and peak aging strengths. Additionally, the addition of Fe could also give a significant effect on the microstructure evolution and mechanical properties of Al–Mg–Si–Cu alloys due to the formation of Fe-rich phases. It has been found that the uniformly distributed Fe-rich phases could weaken the textures, and refine the microstructure of the alloys, and finally improve the formability of Al–Mg–Si–Cu alloys [14–16]. However, if the coarse Fe-rich phases cannot be completely broken into small ones during the thermo-mechanical processing, some micro-cracks can be remained in these coarse particles, and finally reducing the formability and bendability of the alloys [17,18]. Therefore, it is greatly important to control and optimize the formation and distribution of Fe-rich phases in the alloys in order to provide a positive effect on the enhancement of formability and bendability.

Some researchers have shown that the Ni addition can improve the nucleation of Fe-rich phases in the Al–Mg–Si alloys during the casting process due to the interaction between Ni and Fe elements [19,20]. This can further increase the number density of spherical α-Fe-rich phase, and improve the formability of the alloys in the pre-aging state [20].

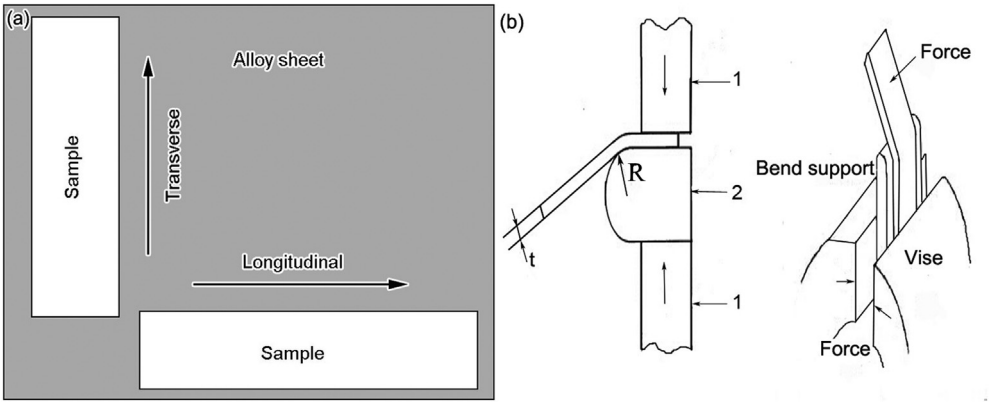

Fig. 2 – Schematics of cutting way of bending sample (a) and semi-guided bend test (b) (1—clamp, 2—former, *t*—thickness of test piece, *r*—radius of the former).

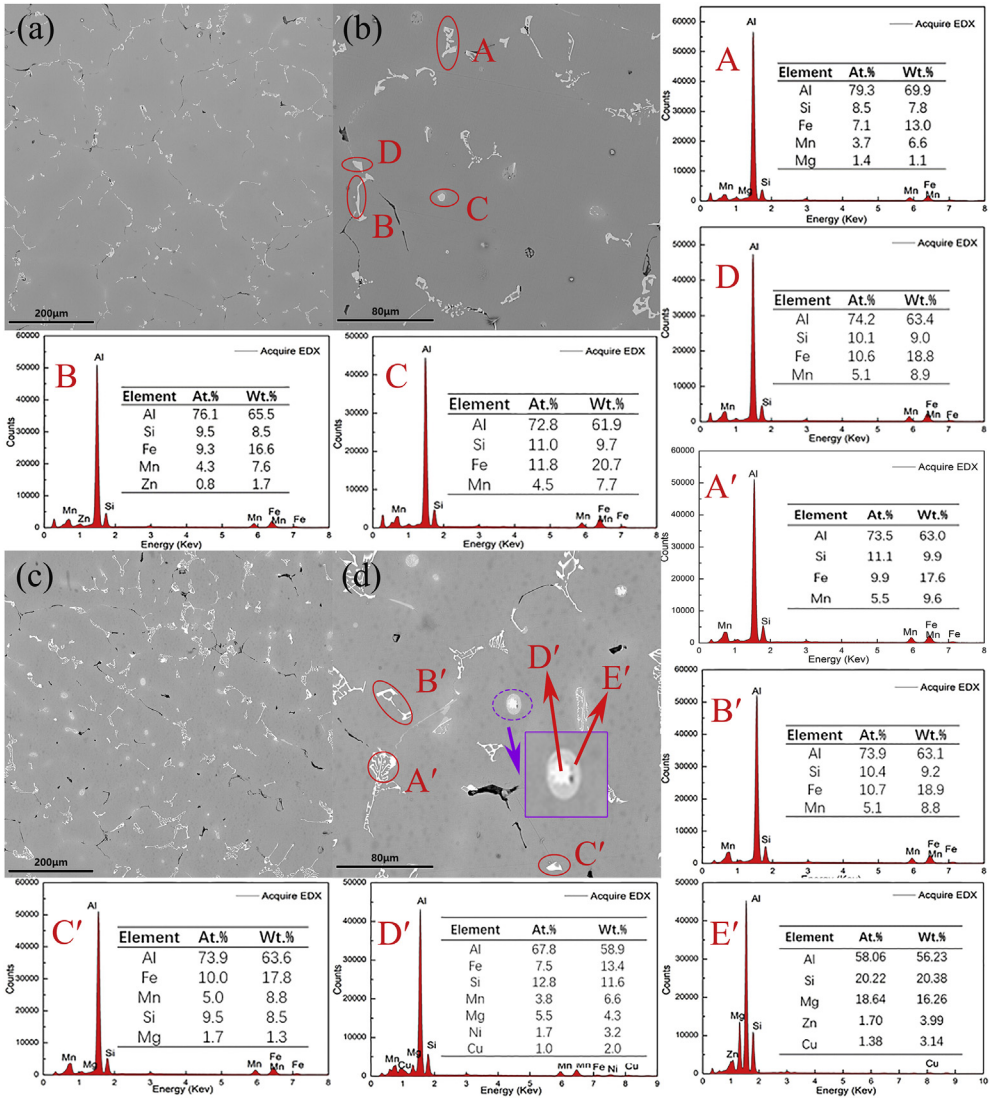

Fig. 3 – SEM microstructure and EDS analysis of the alloys in the as-cast state, (a) (b) #1 alloy, EDS analysis of particles A, B, C and D, (c) (d) #2 alloy, EDS analysis of particles A′, B′, C′, D′ and E′.

However, the detailed study on this topic still needs to be done to further improve the positive effect on the mechanical properties assisted by optimized thermomechanical processing, and better understand the related mechanisms. It has been found that the effect of thermomechanical processing on the microstructure evolution and mechanical properties of Al–Mg–Si–Cu alloys has been widely studied in the past years [20–25], for example, the effects of rolling temperature, rolling reduction, annealing and solution conditions on them. And with increase of annealing time, the size of precipitates can be increased, which further not only affects the microstructure evolution, but also the formability and strength of the alloys in the pre-aging state. However, with the induction of Fe-rich phases in the alloys, the effect of thermomechanical processing parameters on the microstructure and mechanical properties of the Al–Mg–Si–Cu alloys changes greatly due to the complex evolution of Fe-rich phases. Here, if the Ni micro-alloying is used in controlling the nucleation and growth of Fe-rich phases, the effects of Fe-rich phases and thermomechanical processing on the formability and bendability of Al–Mg–Si–Cu alloys should be changed and complex greatly. Thus, the synergy of Ni micro-alloying and thermomechanical processing on the improved phase distribution, formability and bendability of Al–Mg–Si–Cu–Zn–Fe–Mn-(Ni) have been systematically studied in this paper.

2. Experimental

The chemical composition of experimental alloys is as follows (given in wt.%), #1: Al-0.8Mg-1.2Si-0.2Cu-0.5Mn-0.4Fe-3.0Zn and #2: Al-0.8Mg-1.2Si-0.2Cu-0.5Mn-0.4Fe-3.0Zn –0.03Ni. High-purity Al, Al–10Mn, Al–20Si, Al–50Cu, industrial pure Mg, industrial pure Zn, and a grain refining agent Al–5Ti–1B were smelted in an electric resistance furnace and then cast into a water-cooled steel mold at 720 °C to get an ingot with a size of 220 mm (length) × 120 mm

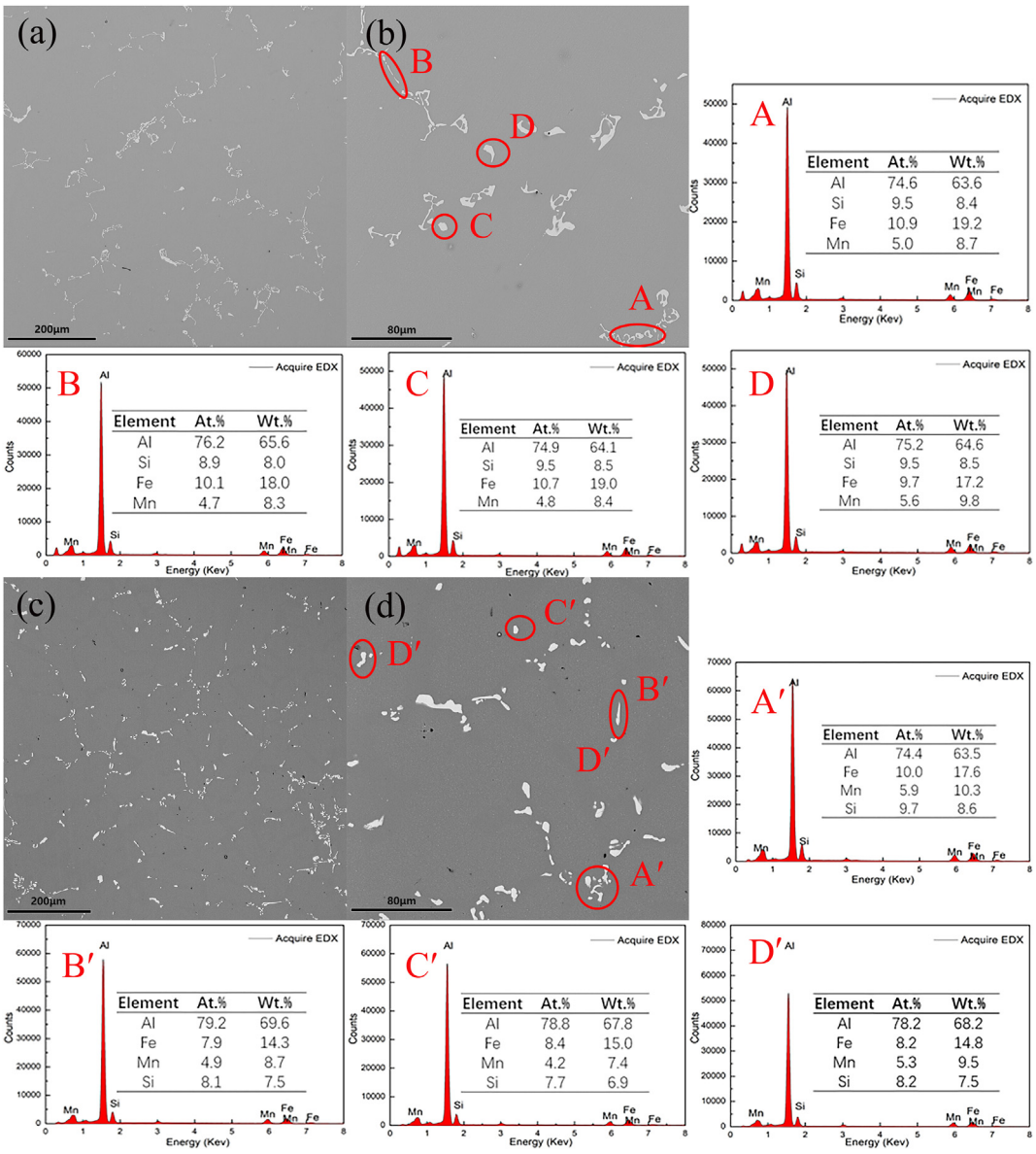

Fig. 4 – SEM microstructure and EDS analysis of the alloys in the homogenization state, (a) (b) #1 alloy, EDS analysis of particles A, B, C and D, (c) (d) #2 alloy, EDS analysis of particles A′, B′, C′ and D′.

(width) × 100 mm(thickness). The ingots were homogenized at 485 °C/3h + 555 °C/30h then milled to remove the outer oxide layer, remaining 90 mm in thickness.

To understand the mechanical properties variation induced by different thermomechanical processing, #2 alloy is divided into two parts: #2-A and #2-B. Firstly, #1 and #2-A

Table 1 – The volume fraction of iron-rich phases with different morphologies and transformation rates of β → α in the alloys in different states.

Alloys	Morphology	Casting state (vol.%)	Homogenization state (vol.%)	β→α transformation rate (%)
#1 alloy	Net-like (β phases)	84.5	62.5	20%
	Rod (β phases)	4.5	7	
	Spherical (α phases)	4	17	
	Irregular shapes (α phases)	6	13.5	
#2 alloy	Net-like (β phases)	85	12	75%
	Rod (β phases)	5	3	
	Spherical (α phases)	3	50	
	Irregular shapes (α phases)	7	35	

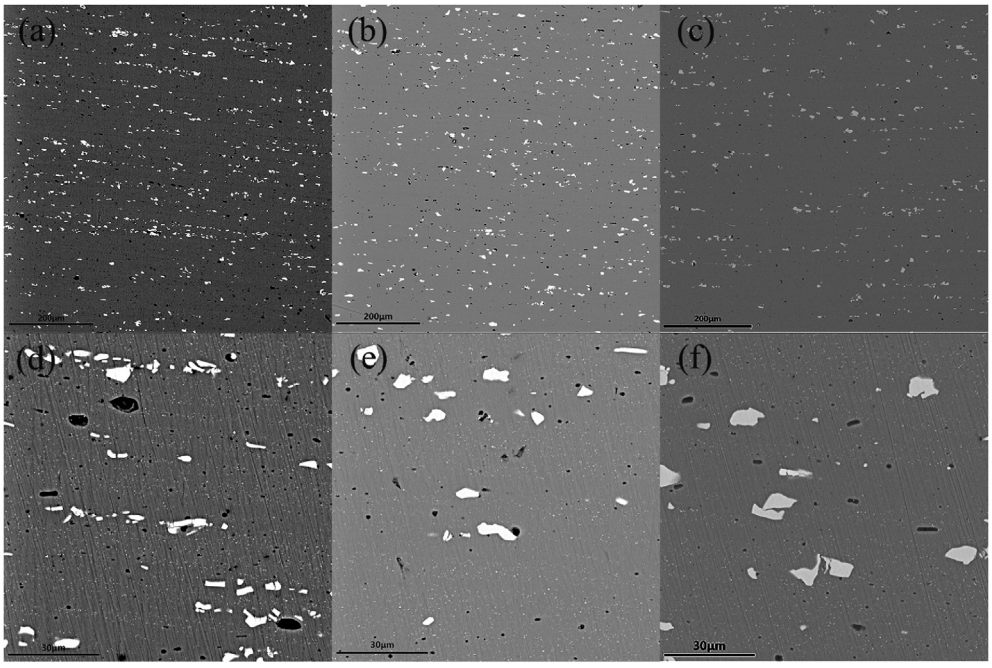

Fig. 5 – SEM microstructure of the alloys in the hot rolling state, (a) (d) #1 alloy, processing route I, (b) (e) #2 alloy, processing route I, (c) (f) #2 alloy, processing route II.

alloys were prepared by the following thermomechanical processing route I: the ingots were hot rolled from 90 to 4 mm (95.6% reduction) → cold rolled to 2 mm (50.0% reduction) → intermediate annealing 400 °C/1h → cold rolled to 1 mm; and then, the #2-B alloy was also prepared by following optimized thermomechanical processing route II: the ingot was hot rolled from 90 to 6 mm (93.3% reduction) → cold rolled to 2 mm (66.7% reduction) → intermediate annealing 400 °C/1h → cold rolled to 1 mm. The final hot rolling temperature was above 300 °C, and cold rolling was done at room temperature (RT). The cold-rolled alloy sheets prepared by both routes were subjected to solution

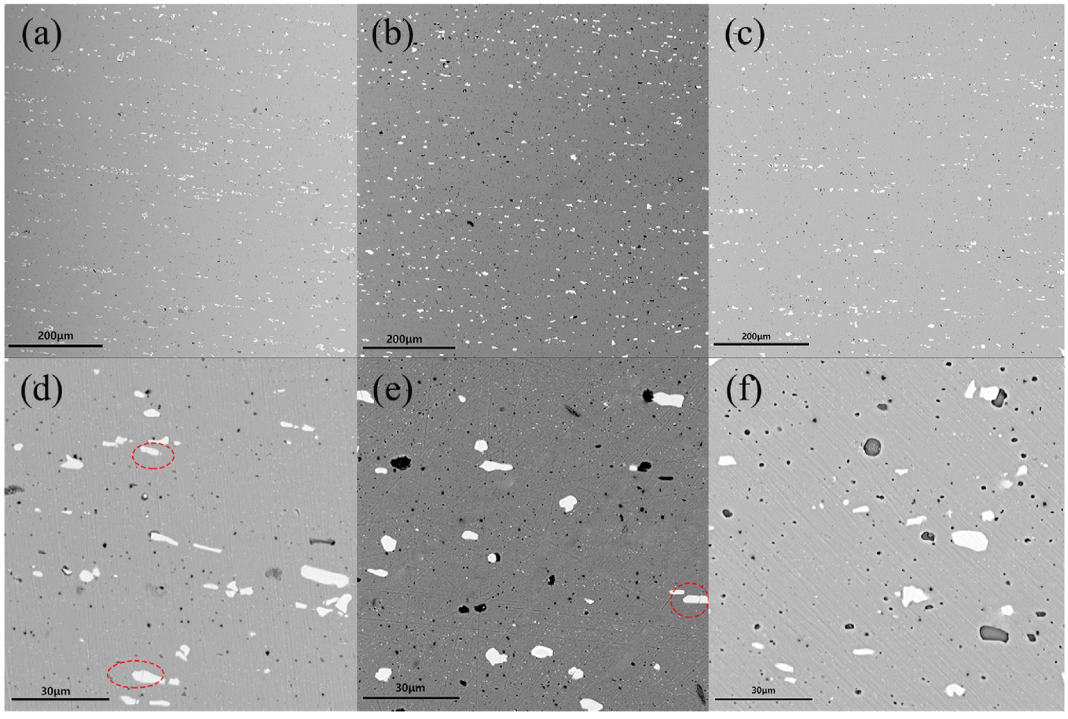

Fig. 6 – SEM microstructure of the alloys in the annealing state, (a) (d) #1 alloy, processing route I, (b) (e) #2 alloy, processing route I, (c) (f) #2 alloy, processing route II.

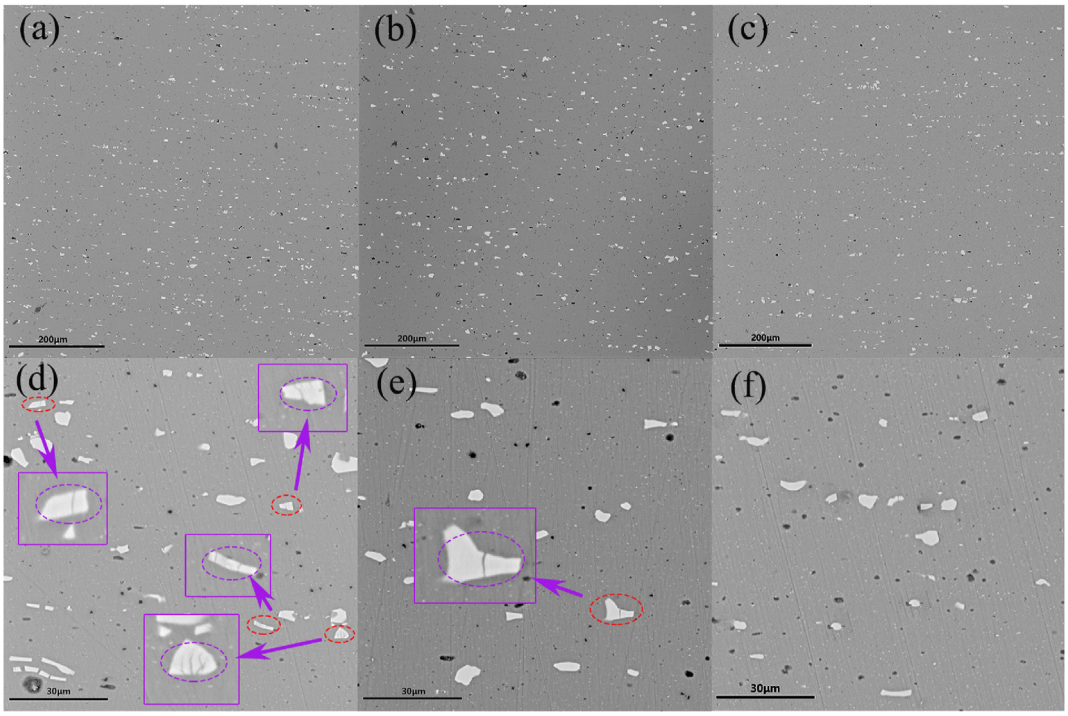

Fig. 7 – SEM microstructure of the alloys in the final cold rolling state, (a) (d) #1 alloy, processing route I, (b) (e) #2 alloy, processing route I, (c) (f) #2 alloy, processing route II.

treatment at 555 °C for 2min in a salt-bath furnace followed by water quenching to RT, and then pre-aged at 80 °C for 12h. The paint baking process is 2% pre-strain + aging at 185 °C for 20 min as shown in Fig. 1.

The tensile test samples were machined from 1 mm cold rolling plates with geometry meeting GB/T228-2002 standard, in directions of 0°, 45° and 90° with respect to the rolling direction. Tensile tests were performed on an MTS800

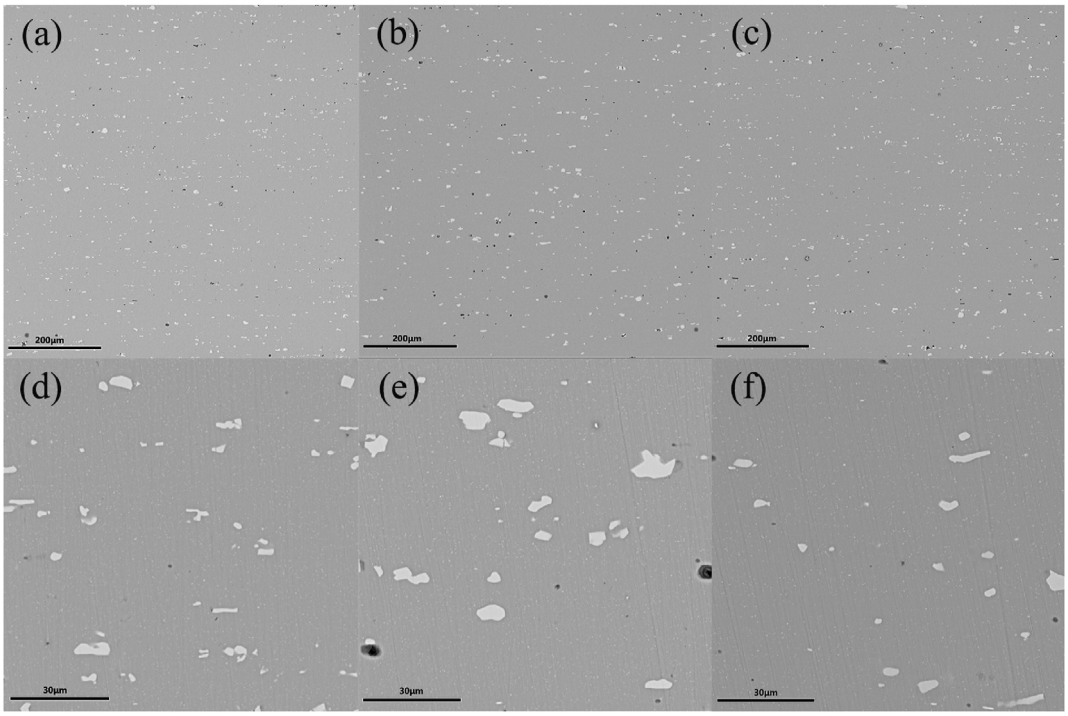

Fig. 8 – SEM microstructure of the alloys in the solution state, (a) (d) #1 alloy, processing route I, (b) (e) #2 alloy, processing route I, (c) (f) #2 alloy, processing route II.

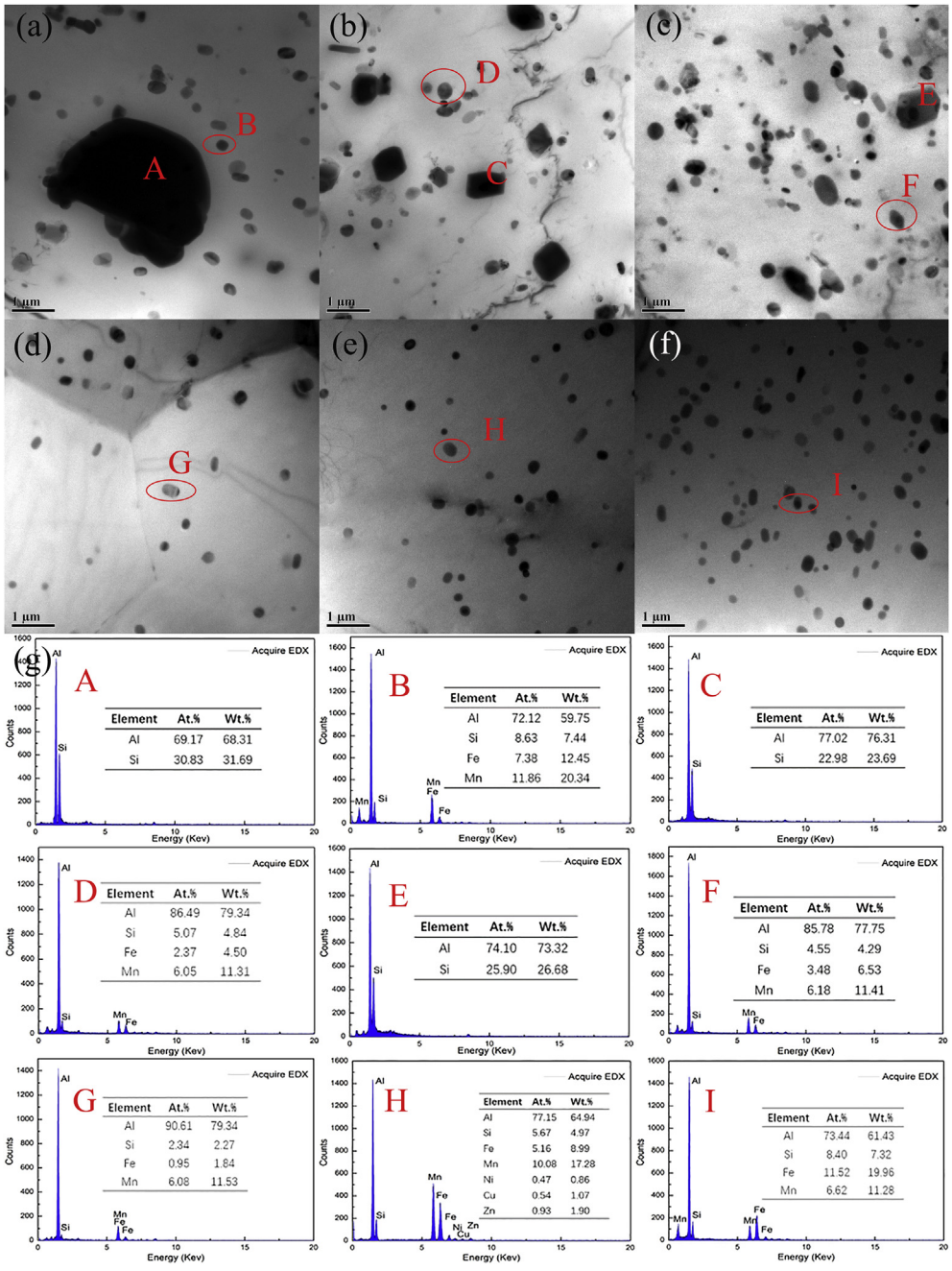

Fig. 9 – TEM microstructure of the alloys in the annealing or solution state, (a) #1 alloy, annealing state of processing route I, (b) #2 alloy, annealing state of processing route I, (c) #2 alloy, annealing state of processing route II, (d) #1 alloy, solution state of processing route I, (e) #2 alloy, solution state of processing route I, (f) #2 alloy, solution state of processing route II, (g) EDS analysis of particles A-I in the alloys.

mechanical tester at a strain rate of 1×10^{-3}/s. The plastic strain ratio (r value) was determined by the 15% offset method, and the average r ($r = (r_0 + 2r_{45} + r_{90})/4$) and plane anisotropy coefficient Δr ($\Delta r = r_0 - 2r_{45} + r_{90})/2$) were calculated. To eliminate unexpected discrepancy, final testing results were collected by averaging three groups of parallel tensile tests in each direction. Nano-indentation experiment was carried out on a MTS Nano Indenter XP. Metallographic samples were prepared by standard metallographic techniques and etched by Keller's reagent (95%vol H_2O+2.5%vol HNO_3+1.5%vol HCl+1%vol HF). The bending performance is usually defined as R/t (where R is the minimum bending radius at which no cracks appear when the sample is bent to 180°, and t is the thickness of the bent sample). The bending specimen size is 20 mm × 70 mm × 1 mm, and the bending test is based on the standard ASTM E290. The samples were taken along the rolling direction and the transverse direction, respectively, and were bent to 180° under the indenter with the same bending radius as shown in Fig. 2.

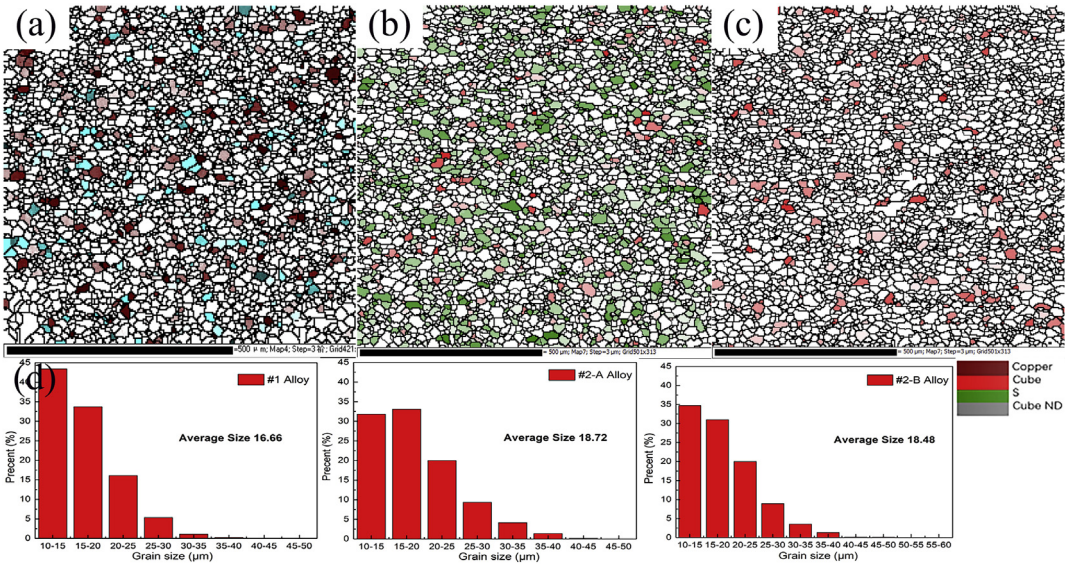

Fig. 10 – EBSD characterization on the texture and grains of the alloys in the solution state, (a) (d) #1 alloy, processing route I, (b) (e) #2 alloy, processing route I, (c) (f) #2 alloy, processing route II.

Table 2 – The texture composition and strength of different alloys after solid solution.

Alloy	Component(texture)	Intensity(F)	Volume fraction(%)
#1	Copper{112}<111>	2.08	6.35
	$Cube_{ND}${001}<310>	4.12	4.14
#2-A	S{123}<634>	2.44	11.8
	Cube{001}<100>	2	4.19
#2-B	Cube{001}<100>	2.68	5.25

The microstructure observation was done on a SUPER 55 scanning electron microscope (SEM) equipped with X-ray energy-dispersive spectrometer (EDS) system. The iron-rich phase particles of two kinds of alloys in solid solution state were characterized on a TecnaiG2 F30 high resolution transmission electron microscopy (HRTEM), along [001] direction of Al matrix, operated at an acceleration voltage of 300 kV. The composition of precipitates was analyzed by equipped EDS system. Specimens were prepared by standard mechanical grinding to a thickness of 100 μm then subjected to twin-jet electro-polishing at −20 °C in mixture solution with 30% HNO_3 and 70% CH_3OH.

3. Results

3.1. *Microstructure evolution*

The microstructure of two alloys in the as-cast state and corresponding composition analysis of precipitates and iron-rich phases are shown in Fig. 2. Casting defects are observed like black pits, inclusions and grooves in both alloys. As can be seen in Fig. 3 (a–d), both alloys have gray primary a-Al grains with equiaxed morphology and bright intermetallic phases with different morphologies. There are two kinds of precipitates: white intermetallic precipitates of spherical, rod, net-like and irregular shapes; white spherical precipitates inside grains. Apparently, the #2 alloy possesses much more net-like phases than that in the #1 alloy. Compared with the #1 alloy, both the increased white spherical precipitates inside grains and the reduced grain size can be also observed in the #2 alloy.

EDS analysis on different phases, i.e. the A-D phases in Fig. 3(b) and the A′-D' phases in Fig. 3(d), shows that the intermetallic precipitates with the different morphologies, are all Fe-rich phase (β or α) in the two alloys; while the spherical Fe-rich phase is mainly the α phase in the #1 alloy (point C), but spherical phase in the #2 alloy is the co-existence of Fe-rich phase (point D′) and Mg–Si phase (Q phase) (point E′). Additionally, composition analysis on the most of spherical phases in the #2 alloy shows that the phases distributed within the grains are the Ni-containing Fe-rich phase as shown in Fig. 3. And the Fe-rich phases are mainly composed of Al–Mn–Si–Fe elements in the two alloys, the Fe content in the Fe-rich phases in the #1 alloy mainly distributes in the range of 7.1–11.8 at.%, while the Fe content in the Fe-rich phases in the #2 alloy is around 10.0 at.%. Accordingly, the Ni micro-alloying gives a significant effect on the composition of Fe-rich phases in the alloys in the as-cast state.

Figure 4 shows the SEM microstructure and EDS analysis on the phases in the alloys after homogenization treatment. It can be seen that the spherical Mg–Si phases observed in the #2 alloy in the as-cast state have been fully dissolved. Although the Fe-rich phases still can be seen in the alloys, yet, the size, morphology and composition have been all changed greatly, as shown in Fig. 3 (a–d). During the homogenization process, some strip and net-like Fe-rich phases observed in the as-cast state have been transformed into some small α-Fe-rich phases with an irregular or spherical morphology (a shown in Fig. 4). Additionally, based on the composition analysis on the Fe-rich phases with different morphologies in both the as-cast and homogenization states, and volume fraction of the different Fe-rich phases, it can be also seen

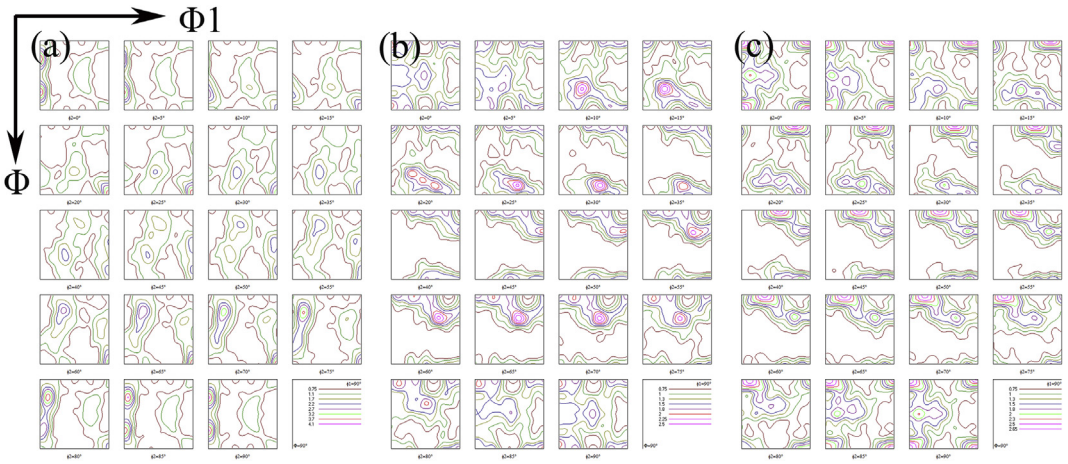

Fig. 11 – ODF pattern of the alloys in solution state, (a) #1 alloy, processing route I, (b) #2 alloy, processing route I, (c) #2 alloy, processing route II.

that, intermetallic phases in the #1 alloy basically have the higher thermal stability, which results in the lower transformation rate of β → α (around 40% transformation rate). While if the micro-alloying Ni is added in the alloy, the spheroidization transformation rate of β → α can be greatly improved (around 75% transformation rate as shown in Table 1), which results in the significantly enhancement of uniform distribution level of Fe-rich phases and number density of fine Fe-rich phases in the #2 alloy. Additionally, based on the EDS analysis results (as shown in Fig. 4), the Fe-rich phases distributed around the grain boundaries in the two alloys after homogenization treatment are almost composed of Al, Mn, Fe and Si elements, and the Fe content in the most of Fe-rich phases is above 10.0 at. % in the #1 alloy, while the Fe content in the Fe-rich phases is below or around 8.4 at. % in the #2 alloy. Accordingly, the Ni micro-alloying not only can improve the transformation rate of β → α, but can also give a significant effect on the composition of Fe-rich phases in the alloys after homogenization treatment.

After hot rolling of the thermomechanical processing I (95.6% reduction), and thermomechanical processing II (93.3% reduction), the microstructure of the alloys changes greatly as shown in Fig. 5. It can be seen that the large-sized Fe-rich phases in the homogenization state are broken and redistributed within the alloy matrix, and forming a multi-scale and uniform distribution characteristics (as shown in Fig. 4). However, with the changes of composition and thermomechanical processing route, the corresponding distribution characteristics also change greatly. The number density of Fe-rich phases in the #2 alloy is lower than that of #1 alloy, which should be resulted from the higher transformation rate of β → α during the homogenization treatment (as shown in Table 1). And if the deformation of hot rolling is changed, the microstructure of the #2 alloy in the hot rolling state is also changed, i.e., the uniform distribution level of the Fe-rich phases increases with the increase of hot rolling deformation, while the size of Fe-rich phases decreases with the increase of hot rolling deformation (as shown in Fig. 5).

And then, if the reduction of cold rolling between hot rolling and annealing is changed, the microstructure of the alloys in the annealing state is also changed greatly (as shown in Fig. 6), especially for the distribution of Fe-rich phases. It can be seen that with the increase of cold rolling reduction, the number density of coarse particles in the #2 alloy treated by the processing route II is decreased compared with the #2 alloy treated by processing route I, and there are much more fine particles in the alloy matrix (as shown in Fig. 6 (c, f)). Accordingly, it can be seen that the thermomechanical processing is greatly important to control and optimize the size and distribution of Fe-rich phases in the alloys.

After the annealing treatment, the #1 and #2 alloys with same processing routes were further cold rolled to the final thickness from 2 mm to 1 mm. The Fe-rich phases observed in the alloys are further broken into the fine particles with a smaller size. However, compared with each other, it can be seen that some micro-cracks are remained in some of the

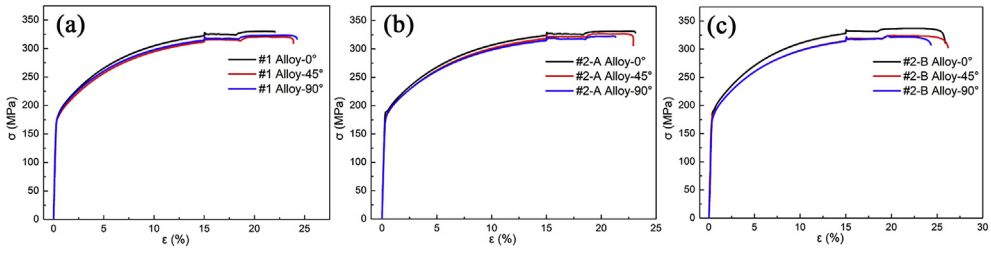

Fig. 12 – The tensile curves of the alloys in the three directions of 0°, 45° and 90° after pre-aging treatment, (a) #1 alloy, (b) #2-A alloy, (c) #2-B alloy.

Table 3 – Mechanical properties of alloys in the pre-ageing state.

Alloy	Direction	r	$\bar{r}$	Δr	n	$\bar{n}$	δ (%)	$\bar{\delta}$(%)	$\sigma_{0.2}$ (MPa)	$\bar{\sigma}_{0.2}$ (MPa)	σ_b (MPa)	$\bar{\sigma}_b$ (MPa)
#1	0°	0.640 ± 0.001	0.679 ± 0.001	−0.10 ± 0.001	0.272 ± 0.001	0.271 ± 0.001	22.28 ± 0.8	25.13 ± 1.0	183.68 ± 1.0	181.37 ± 0.9	330.35 ± 1.2	324.93 ± 1.2
	45°	0.727 ± 0.002			0.273 ± 0.001		27.60 ± 1.2		178.59 ± 0.6		320.92 ± 0.8	
	90°	0.619 ± 0.001			0.267 ± 0.001		25.52 ± 1.0		181.83 ± 1.2		323.52 ± 1.5	
#2-A	0°	0.658 ± 0.002	0.685 ± 0.001	−0.03 ± 0.001	0.268 ± 0.001	0.269 ± 0.001	25.36 ± 1.0	24.99 ± 1.1	190.11 ± 1.6	186.48 ± 1.3	331.48 ± 1.9	326.37 ± 1.5
	45°	0.701 ± 0.002			0.272 ± 0.001		27.00 ± 1.1		183.60 ± 1.2		324.97 ± 1.4	
	90°	0.682 ± 0.001			0.266 ± 0.001		22.60 ± 1.2		185.72 ± 1.2		322.66 ± 1.3	
#2-B	0°	0.628 ± 0.001	0.688 ± 0.001	−0.09 ± 0.001	0.270 ± 0.001	0.269 ± 0.001	26.04 ± 1.0	25.72 ± 1.0	191.82 ± 1.4	186.15 ± 1.4	337.06 ± 1.6	328.26 ± 1.6
	45°	0.733 ± 0.002			0.270 ± 0.001		26.38 ± 1.0		184.34 ± 1.5		324.12 ± 1.8	
	90°	0.658 ± 0.001			0.268 ± 0.001		24.74 ± 0.9		182.28 ± 1.2		323.60 ± 1.3	

coarse particles distributed in the #1 and #2 alloys treated by the processing route I, and it is quite difficult to find them in the #2 alloy treated by the processing route II (as shown in Fig. 7). It has been found that the remained micro-cracks in the coarse particles can give a negative effect on the improvement of formability and bendability of Al alloys [16,18]. Thus, it is greatly important to optimize the size and distribution of multi-scale particles in the Al alloys by a reasonable collocation of hot rolling, cold rolling and annealing.

Figure 8 shows the SEM microstructure of the alloys in the solution state. It can be seen that the precipitates observed in the cold rolling state have been completely dissolved, only the multi-scale Fe-rich phases can be observed in the alloy matrix, the differences in their distribution are basically the same as those in the final cold rolling state (as shown in Fig. 8).

Besides the differences in the particle distribution in the annealing or solution state characterized by SEM, in order to better show the differences in the multi-scale Fe-rich particles in the alloys, it is quite necessary to give a detailed TEM characterization on the fine particles in the alloys (as shown in Fig. 9). It can be seen that both the precipitates and Fe-rich phases can be observed in the alloys in the annealing state, and with the changes of composition and processing route, their distribution is also changed greatly. Ni micro-alloying can help to reduce the size of Si precipitates in the alloys in the annealing state, i.e., the diameter of Si particles is about 3 μm in the #1 alloy, but only around 1 μm in the #2 alloys treated by processing routes I and II. While the changes of size and distribution of Fe-rich phases in the #1 and #2 alloys treated by the processing route I are both slight. Compared with the processing I, the number density of fine precipitates and Fe-rich phases #2 alloy treated by processing II is increased greatly (as shown in Fig. 8). Additionally, based on the EDS analysis on the Fe-rich phases, the solute concentrations in the Fe-rich phases in the Ni micro-alloying-containing alloys (#2) are all much lower than those of Ni-free alloy (#1), which is basically the similar as the observed composition change in the homogenization state.

Additionally, the Si precipitates observed in the annealing state have been completely dissolved after the solution treatment, and only fine Fe-rich phase particles can be seen in the solution state. And with the changes of composition and processing route, the number density and distribution of fine Fe-rich phases in the alloys also change greatly, the highest number density can be seen in the #2 alloy treated by the processing route II (as shown in Fig. 9). Based on the EDS on the fine particles (i.e., G, H and I particles), it can be found that the composition of those particles is different from each other. The composition of Fe-rich phase in the #1 alloy is Al-2.34Si-0.95Fe-6.08Mn (at. %), while the Fe-rich phases in the #2 alloys are changed to the phases of Al-(5.7/8.4) Si- (5.1/11.5) Fe-(10.8/6.6) Mn (at. %). It can be seen that the concentrations of Si, Fe and Mn in the Fe-rich phase distributed in the #2 alloys after solid solution treatment are all much higher than those of #1 alloy. Furthermore, a small amount of Ni element has been also detected in some Fe-rich phase particles in the #2 alloy treated by the processing route I, which indicates that the formation and growth of multi-scale Fe-rich phases are really affected by the Ni micro-alloying. This also gives a further influence on the evolution of Fe-rich phases during the

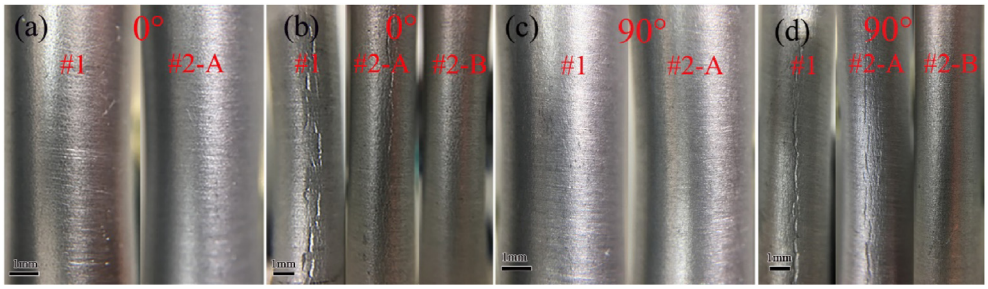

Fig. 13 – Surface analysis of the pre-aging treated alloys after bending with different deformations, (a) #1 and #2-A alloys, R/t = 2, 0° direction, (b) #1, #2-A and #2-B alloys, R/t = 1, 0° direction, (c) #1 and #2-A alloys, R/t = 2, 90° direction, (d) #1, #2-A and #2-B alloys, R/t = 1, 90° direction.

thermomechanical processing. Thus, the different distribution characteristics of multi-scale Fe-rich phases in the #2 alloys treated by the processing routes I and II can be formed as shown in Figs. 8 and 9.

3.2. *Microstructure and texture characterization after solution treatment*

The observed different distribution characteristics of multi-scale particles in the alloys could give a significant effect on the recrystallization behaviors during the solution treatment. Thus, it is necessary to give a detailed EBSD characterization on the alloys to show their microstructure and texture changes with the changes of composition and thermo-mechanical processing. Figure 10 shows the EBSD microstructure of the alloys in the solution state. It can be seen that the complete recrystallization has been occurred in the alloys after the solution treatment, and lots of equiaxed recrystallization grains can be seen in the alloy matrix. The grain size of the alloys mainly distributes in the range of 10–20 μm, and the average size of the recrystallization grains in the #1, #2 alloys treated by processing I and II is 16.66, 18.72 and 18.50 μm, respectively. The higher average grain size in the #2-A and #2-B alloys is mainly resulted from the appearance of some coarse grains in the alloys. And the co-existence of fine and coarse recrystallization grains is most prominent in the #2 alloy treated by the processing route II. Accordingly, the multi-scale grain size distribution has been formed in the alloys by the help of synergy of Ni micro-alloying and thermomechanical processing.

Besides the differences in the grain distribution in the alloys, the texture distribution also changes greatly in the alloys (as shown in Table 2). It can be seen that the rolling texture of the #1 alloy mainly includes Copper texture with a volume fraction of 6.35%, and recrystallization texture $Cube_{ND}$ with a volume fraction of 4.14% has been also formed in the alloy; while the rolling texture S with a volume fraction of 11.8%, and recrystallization texture Cube with a volume fraction of 4.19% are both formed in the #2 alloy treated by the processing route I. However, with the change of processing route, only the recrystallization texture Cube with a volume fraction of 5.25% can be seen in the #2 alloy treated by the processing route II. Accordingly, we can find that both the Ni micro-alloying and cold rolling reduction between hot rolling and annealing also give a significant effect on the texture evolution during the solution treatment. The detailed evolution mechanisms can be found in the following part.

3.3. *Mechanical property characterization*

With the changes of microstructure and texture in the alloys, the mechanical properties of the alloys should be also changed greatly. Figure 12 shows the tensile curves of the alloys in the pre-aging state (80 °C/12hrs) along the directions of 0°, 45° and 90° respect to the rolling direction, and the corresponding mechanical properties are shown in Table 3. It can be seen that the yield strengths ($\sigma_{0.2}$) of the alloys in the three directions are similar with each other, corresponding to the lower anisotropy. With the addition of micro-alloying Ni in the alloys, the yield strength ($\sigma_{0.2}$) of the alloys is increased from 181.37 MPa (#1) to 186.48 MPa (#2-A) and 186.15 MPa (#2-B), and the ultimate tensile strength (σ_b) is also improved slightly (as shown in Table 3). A small difference in the elongation of the alloys can be found, and basically the highest elongation value appears in the #2 alloy treated by the processing route II. Besides these differences, the formability of the alloys is also

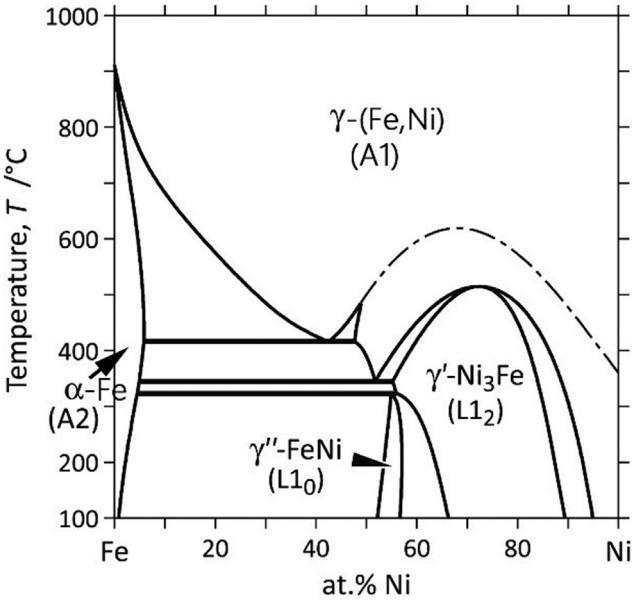

Fig. 14 – Phase diagrams of the Fe–Ni binary system [27].

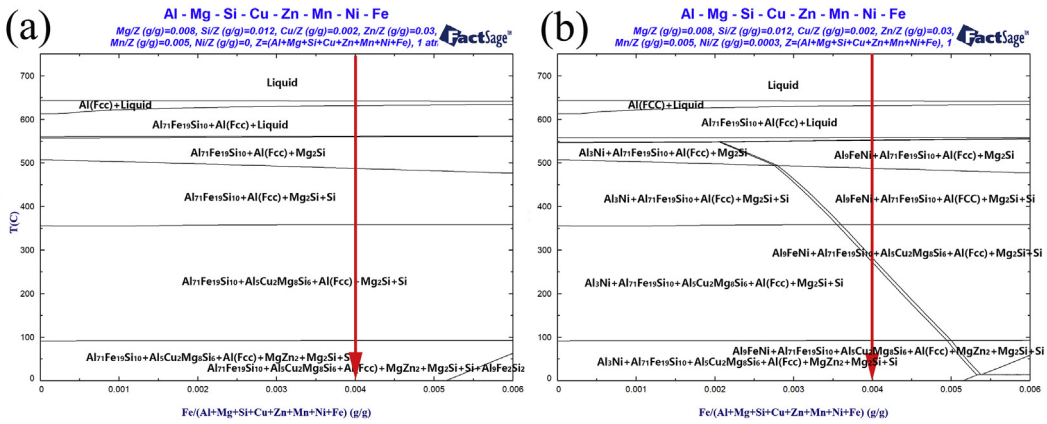

Fig. 15 – Phase diagram of different Fe added to Al–Mg–Si–Cu–Zn–Mn(-Ni) alloy with or without Ni, (a) Free-Ni alloy, (b) Ni-containing alloy.

affected by the synergy of Ni micro-alloying and thermomechanical processing, and the highest average r value appears in the #2 alloy treated by the processing route II (as shown in Table 3).

In addition, the distribution of Fe-rich phases also gives a significant effect on the improvement of bendability of the Al alloys. Figure 13 shows the surface quality of the alloys in the pre-aging state after bending with different deformations. It can be seen that the surface quality of the #1 and #2 alloys treated by the processing route I has a slight difference in both the longitudinal and transversal directions only after the bending deformation reaching R/t = 1, i.e., much more micro-cracks being formed in the #1 alloys compared with the #2 alloy; and if the #2 alloy is treated by the processing route II, the surface of the alloy sheet after the bending with a deformation of R/t = 1 has not any micro-cracks (as shown in Fig. 13 (b, d)). Accordingly, it can be seen that even the #2 alloys treated by the processing routes I and II have a similar average r (as shown in Table 2), the bendabilities of them are quite different from each other. This further indicates that the synergy of Ni micro-alloying and thermomechanical processing is greatly important to enhance the microstructure, texture, formability and bendability of Al–Mg–Si–Cu–Zn–Fe–Mn alloys.

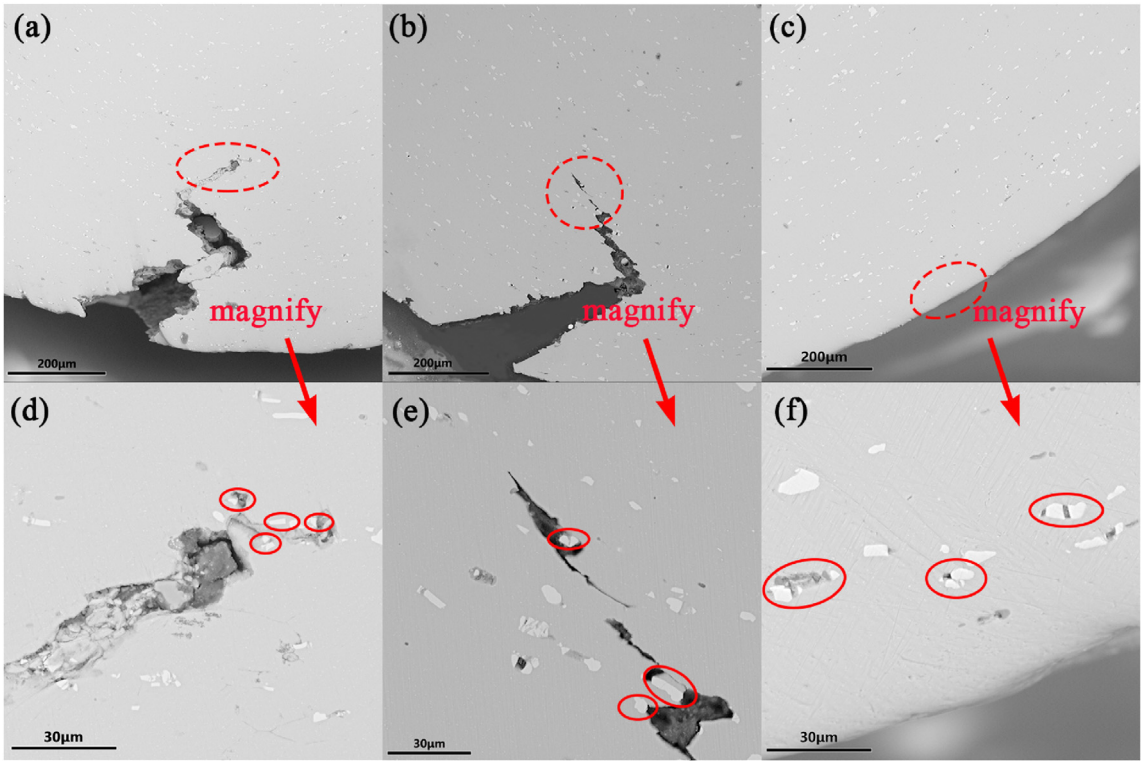

Fig. 16 – SEM microstructure of the pre-aged alloy sheets after bending along rolling direction with a deformation of R/t = 1, (a) (d) #1 alloy, processing route I, (b) (e) #2 alloy, processing route I, (c) (f) #2 alloy, processing route II.

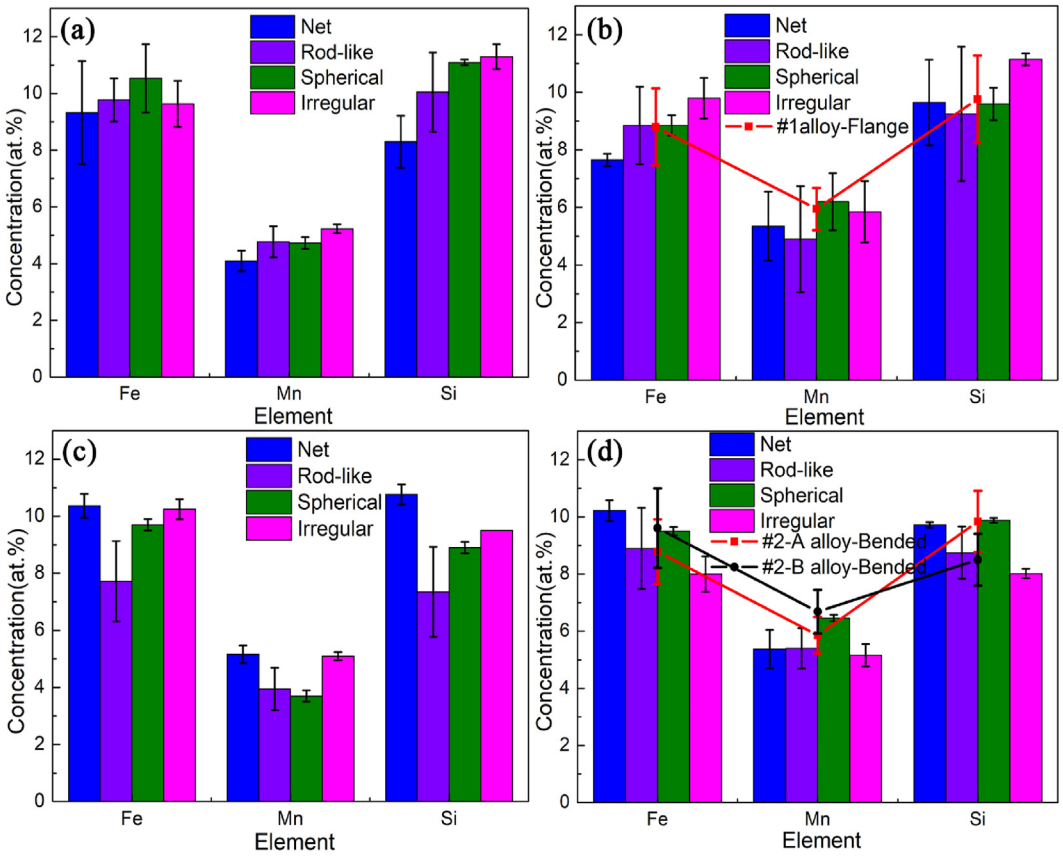

Fig. 17 – Composition statistics of Fe-rich phases distributed in the alloys in the different conditions, (a) #1 alloy, as-cast state, (b) #1 alloy, homogenization state and the Fe-rich phase around the flange crack, (c) #2 alloy, as-cast state, (d) #2 alloy, homogenization state and the Fe-rich phase around the flange crack.

4. Discussion

4.1. *Theoretical basis of Ni micro-alloying design*

Considering the fact that size and distribution of Fe-rich phases give a significant effect on the microstructure evolution and mechanical properties of Al alloys, an appropriate micro-alloying element should be selected and used to control the nucleation and growth of Fe-rich phases during the casting process. Based on the phase diagram of Fe–Ni system (as shown in Fig. 14) [27], it can be seen that a compound of γ-(Fe, Ni) (A1) phase is easily formed in the high temperature, indicating the strong interaction between Fe and Ni is existed. Thus, if the Al–Mg–Si–Cu–Zn–Fe–Mn alloy is added micro-alloying Ni, the Ni should be reacted with Fe-rich phases, and greatly improve the nucleation of Fe-rich phases during the casting process, which can be shown by the improved microstructure of the alloy in the as-casting state (as shown in Fig. 3).

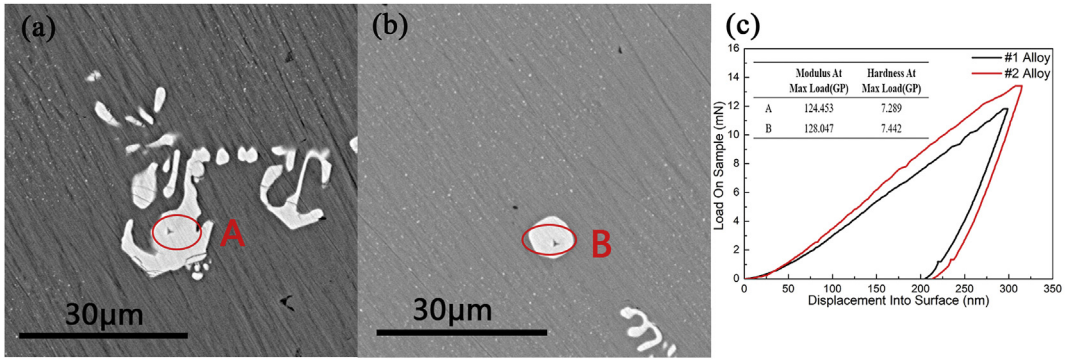

Fig. 18 – Nano indentation photos of different alloys in the homogenized state of Fe-rich phase, (a) #1 alloy, (b) #2 alloy, (c) pressure loading and unloading diagram and corresponding Fe-rich phase strength.

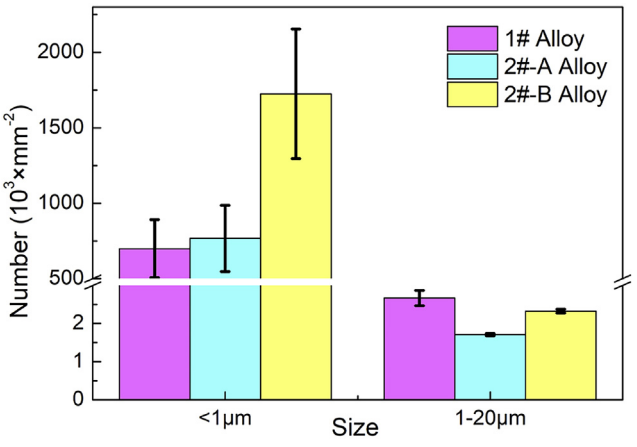

Fig. 19 – Distribution diagram of the second phase particles with different sizes in the final cold rolling state.

Additionally, in order to understand the effect of Ni micro-alloying on the formation of Fe-rich phases, the corresponding phase zone changes are also calculated by FactSage software 7.1. Figure 15 shows the phase diagrams of the Al–Mg–Si–Cu–Zn–Fe–Mn-(Ni) alloys. The computation conditions are described as follows, one bar pressure, the concentration of solute elements (given in wt.%) in Ni free alloy: 0.8Mg-1.2Si-0.2Cu-0.5Mn-(0–0.6) Fe; the concentration of solute elements in the Ni-containing alloy: 0.8Mg-1.2Si-0.2Cu-0.5Mn-(0–0.6) Fe-0.03Ni. From them, it can be seen that Fe-rich phases can be formed in the Ni-free at first below 620 °C; and then Mg_2Si and Si phases can be formed at around 550 °C and 500 °C, respectively; finally, if the temperature is below 350 °C, the corresponding phase zone of $Al_{71}Fe1_9Si_{10}$+$Al_5Cu_2Mg_8Si_6$ +Al(Fcc)+$MgZn_2$+Mg_2Si + Si can be observed (as shown in Fig. 15). For the Ni-containing alloy, the phase zones at the different temperatures are changed with the change of Fe content. It is important that the Al_9FeNi phase can be formed at the temperature of below 550 °C, and then with the decrease of temperature, the kind of phases also changes, which is significantly different from those in Ni-free alloy. Accordingly, Ni micro-alloying could really give an influence on the nucleation and growth of Fe-rich phases during the casting, homogenization and thermomechanical processing even the content of Ni micro-alloying is only 0.03 wt.%.

According to the results mentioned above, the Ni micro-alloying can really give a significantly effect on the microstructure evolution of Al–Mg–Si–Cu–Zn–Fe–Mn alloy. And Ni-containing Fe-rich phases can be observed in the Al–Mg–Si–Cu–Zn–Fe–Mn–Ni alloy in the as-cast state. After homogenization treatment, although Ni element is not observed in the Fe-rich phases, yet, the Ni-containing Fe-rich phases should still exist in the alloy matrix because some fine Ni-containing Fe-rich phases can be found in the TEM microstructure of the alloy in the solution state (as shown in Fig. 8).

4.2. *Effect of Fe-rich phase morphology on mechanical properties*

With the changes of composition and thermomechanical processing, the morphology of Fe-rich phases changes greatly, which further gives a significant effect on the mechanical properties of the alloys, especially for the bendability (as shown in Fig. 13). In order to better understand its effect, Fig. 16 shows the SEM microstructure of the pre-aged alloy sheets after bending along rolling direction with a deformation of R/t = 1. It can be seen that besides the cracks distributed on the cross section of #1 alloy and #2-A alloy after bending, some micro-cracks also can be found in some coarse Fe-rich phases similar with the results shown in Refs. [18,26,28], and these coarse Fe-rich phases with irregular or rod-like shape mainly distribute around the cracks formed after bending. However, the surface of the #2-B alloy treated by processing II after bending (R/t = 1) is basically smooth, and no cracks or micro-cracks can be found on the surface of the bended alloy sheet (as shown in Fig. 16(c)). Certainly, some microporous or fine holes can be still observed occasionally in some irregular Fe-rich phases (as shown in Fig. 16(f)). Accordingly, the bendability of the alloys or the formation of cracks after bending is closely related with the morphology of Fe-rich phases. With the synergy of Ni micro-alloying and thermomechanical processing, the morphology of Fe-rich phases in the #2 alloy treated by processing route II has been improved greatly, and the number density of Fe-rich phases with irregular or rod-like shape has been also greatly reduced, which finally results in the improvement of bendability of #2-B alloy treated by processing route II.

In order to know the evolution of Fe-rich phases from the as-cast state to the final state, the composition of the Fe-rich phases with different morphologies has been analyzed in a detailed way (as shown in Fig. 17). In the as-cast and homogenization states, the morphology of the Fe-rich phases mainly includes four shapes, i.e., net-like, rod-like, irregular and spherical. A significant difference in the compositions of these four types of Fe-rich phases can be seen (as shown in Figs. 3, 4 and 17). It has been found that the β-Fe-rich phase can be transformed into α-Fe-rich phase during the high temperature homogenization treatment [29,30], and much more spherical Fe-rich phases can be formed in the alloy matrix. And with the occurrence of phase transformation, the corresponding composition of Fe-rich phases also changes greatly, i.e., Al_5FeSi for β phase, and $Al_{15}(FeMn)_3Si_2$ for α phase.

Here for the #1 alloy, the concentrations of Fe, Mn and Si elements change with the change of Fe-rich phase morphology. In the as-cast state, the concentration of Fe element in the spherical Fe-rich phases is the highest among them, while the highest and the lowest concentrations of Si element in the Fe-rich phases appear in the irregular and net-like Fe-rich phases (as shown in Fig. 17(a)). After homogenization treatment, the concentrations of solute elements in the Fe-rich phases also changes, besides the concentration changes of Fe and Si elements, the changed Mn concentration should be mainly resulted from the phase transformation of β → α. For the Ni-containing #2 alloy, the concentrations of Fe, Mn and Si elements in the Fe-rich phases are significantly different from those of Fe-rich phases formed in the #1 alloy, which indicates that the nucleation and growth and Fe-rich phases and Mg–Si precipitates were all affected by the Ni micro-alloying. And the highest Si concentration in the Fe-rich phases with net-like shape can be observed (as shown in Fig. 17(c)). After the homogenization, the concentration of

Mn element in the Fe-rich phases is also changed, especially for the spherical phases. This is mainly resulted from the increased transformation rate of β → α due to the addition of Ni micro-alloying. Considering the fact that the composition of Fe-rich phases is difficultly changed in the processes followed after the homogenization treatment due to low temperature and short time heat treatment being used during them. Thus, according to the composition analysis on the Fe-rich phases distributed around cracks or causing the occurrence of cracking after bending deformation (as shown in Fig. 17), it can be seen that the concentration of Fe, Mn and Si elements in the Fe-rich phases around the cracks in the #1 and #2-A alloy sheets after bending mainly distributes near the solute concentration values of rod-like phases, thus, we can simply conclude that these Fe-rich phases should be formed by the fragmentation of large rod-like or net-like Fe-rich phases. In comparison, the solute concentrations of Fe-rich phases in the #2-B alloy sheet after bending is basically the same as those of spherical phases analyzed in the homogenization state. The number density of spherical Fe-rich phases is greatly increased in the #2-B alloy, causing the improved bendability. Thus, the key role of synergy of Ni micro-alloying and thermomechanical processing is to improve the formation of spherical Fe-rich phases, and finally results in the enhancement of formability and bendability of Al–Mg–Si–Cu–Zn–Fe–Mn alloy.

In order to show the positive effect of spherical Fe-rich phases on the formability and bendability of the alloys, the mechanical properties of some typical Fe-rich phases were characterized by nano indentation tests (as shown in Fig. 18). It can be seen that both the modulus and hardness of the spherical Fe-rich phases distributed in the #2 alloy are higher than those of net-like Fe-rich phases distributed in the #1 alloy. Accordingly, the Ni micro-alloying really gives a significant effect on the nucleation, growth, phase transformation and mechanical properties of Fe-rich phases in the alloys. And finally, based on the synergy of Ni micro-alloying and thermomechanical processing, the phase distribution, formability and bendability of Al–Mg–Si–Cu–Zn–Fe–Mn alloys can be all greatly improved.

4.3. *Effect of Fe-rich phases distribution on recrystallization*

Based on the results mentioned above, it can be found that the differences in size and distribution of the Fe-rich phase could give an important influence on the microstructure evolution during high temperature heat treatments. Besides the fragmentation of coarse Fe-rich phases changing the size and distribution of them, the long monoclinic β-Al_5FeSi phases in the Al alloys can also transform into spherical cubic α-$Al_{15}(FeMn)_3Si_2$ phases after high temperature homogenization treatment to change their size and distribution [29,30]. The driving force of the phase transformation comes from the difference in surface composition between α-Fe-rich phase and β-Fe-rich phase. It has been believed that Mn element can improve the transformation rate of the phases, and the transformation rate is mainly controlled by the Fe element due to its low diffusivity rate [31–33]. Thus, the influence of Mn and Si in the diffusion process can be ignored, and only the solubility changes of Fe atoms in the two Fe-rich phases are considered, as follows [31]:

$$V\mu = \mu_{\beta}^{S} - \mu_{\alpha}^{S} \tag{1}$$

here, $V\mu$, difference in composition, the solute Fe in the matrix close to interface of β (μ_{β}^{S}) and α (μ_{α}^{S}), assuming that the surface solubility of the two Fe-rich phases can quickly reach dynamic equilibrium. After a period of transformation, the conversion ratio of the α-Fe-rich phase is $f(\alpha)$ [31,34]:

$$f(\alpha) = \frac{V(\alpha)}{V(\alpha) + V(\beta)} = \frac{\frac{4}{3}\pi R^3}{\frac{4}{3}\pi R^3 + \pi l^2 d} \tag{2}$$

here, V(α), V(β) are volume fractions of the α phase and β phase in the Al matrix, respectively, R is the radius of the α phase, and l, d are radius and thickness of β phase (assuming a columnar phase). So the smaller β phase can easily transforms into more α phase in the same time at the same temperature. As shown in Fig. 2(a) and (c), the morphology of Fe-rich phases in the #1 alloy is mainly slender strip and few net; the net composed of finer rod-like or independent small particles in the #2 alloy. Additionally, some extra particles (Q, Al–Fe–Ni phases) offer more nucleation to α phase in #2 alloy at the transformation process. All of these directly results in the higher transformation rate of Fe-rich phases in the #2 alloy, and much more spherical α-phases can be found in the #2 alloy in the homogenization state (as shown in Fig. 3(a, c)).

The formed Fe-rich phases are relatively stable, and no changes of structure and composition can be found during the following hot rolling, cold rolling, annealing and solution treatments [35]. Certainly, those coarse Fe-rich phase can be broken into some smaller ones, and finally forming co-existence of fine and coarse Fe-rich phases, or multi-scale distribution characteristics. With the change of distribution characteristic, the recrystallization behavior of the alloys also changes greatly during the solution treatment. It has been found that coarse particles (>1 μm, such as, Fe-rich phases) improve the nucleation of recrystallization grains (PSN effect), and weaken the rolling texture, while fine particles (<1 μm, such as, Mg_2Si, Si, Q, Fe-rich phases) can retard the growth of recrystallization grains [24,36–38]. The corresponding critical size of particle to induce the occurrence of PSN effect can be expressed as follows [39],

$$d_{crit} = \frac{4\gamma_b}{P_D - P_Z} = \frac{4\gamma_b}{\left(\alpha\rho G b^2 / 2\right) - \left(3F_v\gamma_b / d_p\right)} \tag{3}$$

where γ_b is specific grain boundary energy; P_D is the deformation storage energy; P_Z is pinning force of the second small particles; the terms F_V, d_p are the volume fraction and diameter of the small particles; ρ and G are the number density of dislocation and shear modulus. According to the Eq. [3], d_{crit} increases with the decreasing P_D or increasing P_Z. Therefore, the distribution of Fe-rich phases should be better controlled to positively affect nucleation and growth of recrystallization grains.

Figure 19 shows the concentration distribution of Fe-rich phases with different sizes in the alloys in the final cold

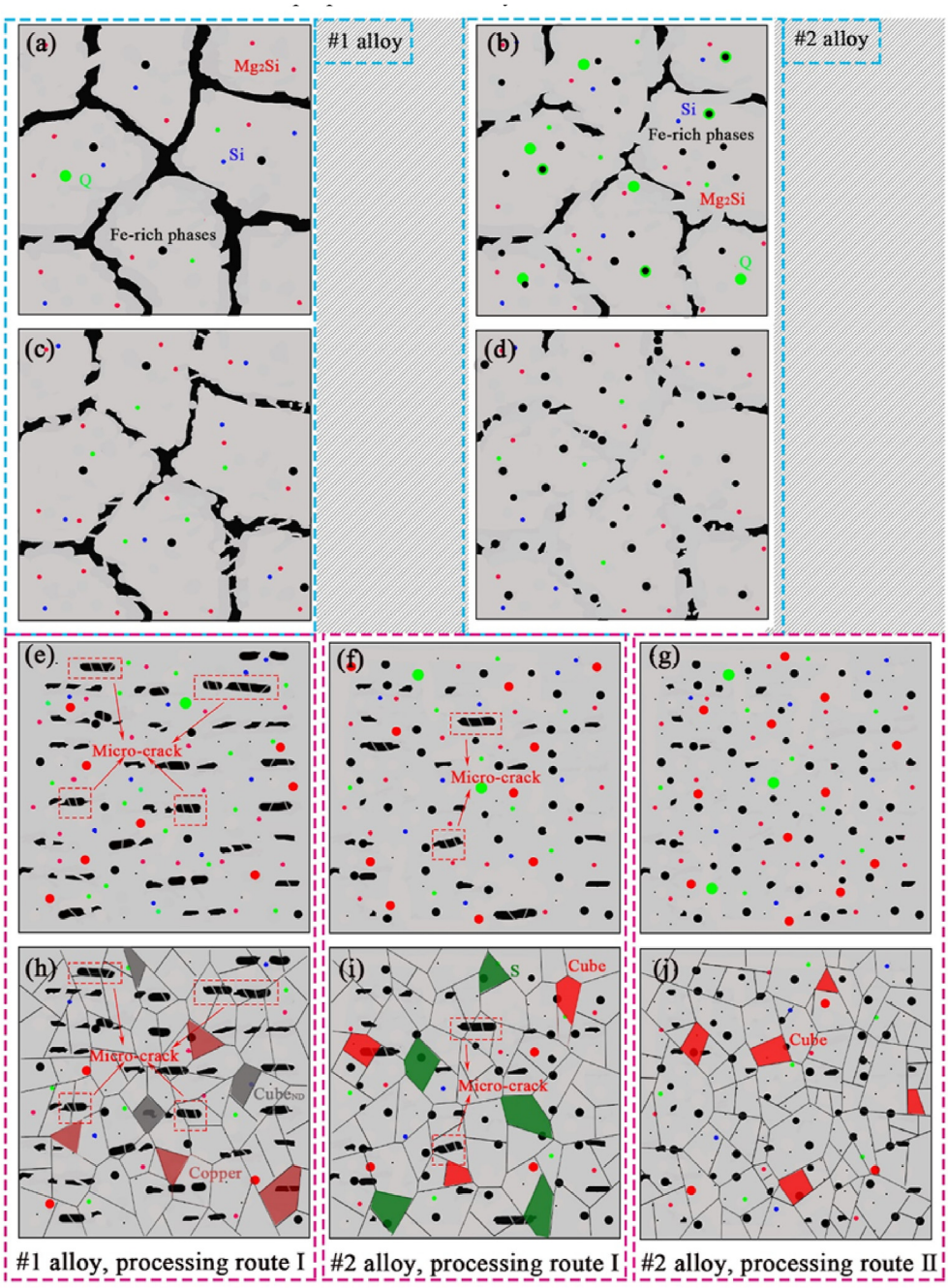

Fig. 20 – Schematic diagram of the Fe-rich phases particles evolution of Al–Mg–Si–Cu–Zn–Fe–Mn(-Ni) alloys (a) (b) #1 and #2 alloys in the as-cast state, (c) (d) #1 and #2 alloys in the homogenization state, (e)–(g) #1, #2-A and #2-B alloys in the final cold rolling state, (h)–(j) #1, #2-A and #2-B alloys in the solution state.

rolling state. It can be seen that the concentration of small particles (<1 μm) in the #1 alloy is slightly less compared with the other two alloys, while the concentration of coarse particles (>1 μm) is obviously higher than that of #2-A alloy. Accordingly, the pinning effect of fine particles in the #1 alloy should be weaker than that of the #2-A alloy, which results in the different recrystallization microstructure and texture distribution in the alloys (as shown in Figs. 10 and 11, Table 2). With the change of thermomechanical processing parameters (i.e., cold rolling deformation between hot rolling and annealing), the distribution of Fe-rich phases in the #2-B alloy also changes greatly (as shown in Fig. 19), that is, the number density of fine particles is greatly increased. These increased fine particles can better retard the growth of recrystallization grains during the solution treatment, and finally resulting in the improvements in the microstructure of the #2-B alloy. Besides, the improved the microstructure, the texture evolution is also significantly affected by the formed Fe-rich phases in the cold rolled alloys. With the help of Fe-rich phases and changed thermomechanical processing, only the Cube texture

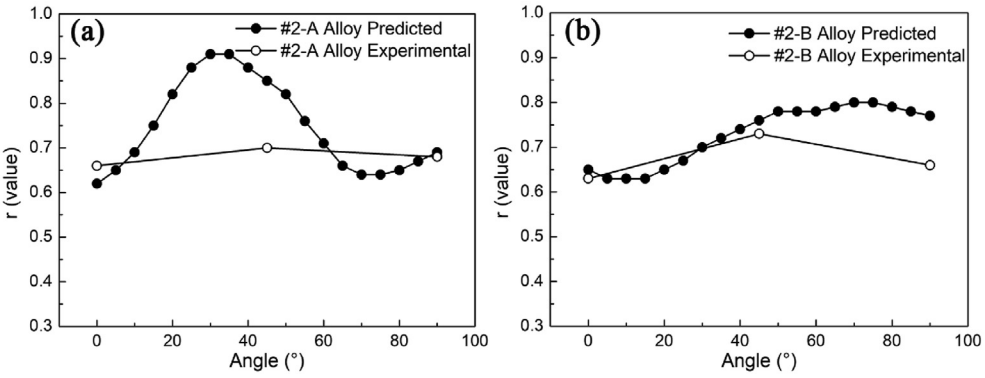

Fig. 21 – Experimental and predicted r value of the #2 alloys treated by processing routes I and II, (a) #2-A alloy, processing route I, (b) #2-B alloy, processing route II.

with a low volume fraction can be observed in the #2-B alloy sheet after solution treatment. And finally, the formability and bendability of the #2-B alloy treated by processing route II are greatly improved.

4.4. *Synergy of Ni micro-alloying and thermomechanical processing*

The improved mechanical properties of the alloys are mainly resulted from the synergy of Ni micro-alloying and thermomechanical processing. Thus, it is necessary to give a discussion on their synergy mechanism. The formation and transformation of Fe-rich phases in Al–Mg–Si-(Cu) alloys have been extensively studied [29,30,40], but the influence of the addition of Ni element on the Fe-rich phases is still not completely understood [20]. Accordingly, the corresponding Fe-rich phases particles evolution of Al–Mg–Si–Cu–Zn–Fe–Mn-(Ni) alloys is put forward as shown in Fig. 20. In the as-cast state, the Ni-containing Fe-rich phase (e.g. Al–Fe–Ni phases, black spots (slighter small)) and Mg–Si phases (e.g. Q phases, green spots) can be formed in the #1 and #2 alloys, and some Q phases can be also formed around the Al–Fe–Ni phase, which results in the higher number density of Q phase in the #2 alloy. Moreover, there are some small Mg_2Si phase (red dots) and Si particles (blue dots) in the two alloys in the as-cast state (as shown in Figs. 3 and 20). After homogenization treatment, although Mg–Si precipitates (such as, Q, Mg_2Si and Si phases) can be dissolved, yet, they can also act as nucleation sites for the phase transformation from β-Fe-rich phases to α-Fe-rich phase [41,42]. Thus, the transformation from β-Fe-rich (strip and network-like) to α-Fe-rich (spherical) particles in the #2 alloy can be improved by the help of the precipitates (as shown in Table 1). Certainly, the improved transformation rate from β to α is also resulted from the changed composition and distribution of Fe-rich phases in the #2 alloy with the help of Ni micro-alloying.

After the homogenization treatment, if the #1 and #2 alloys are treated by the processing route I, although the coarse Fe-rich phases in the two alloys can be broken into many fine particles, and forming the distribution characteristic of multi-scale Fe-rich phases in the final cold rolling state, yet, a significant difference in the final distribution of multi-scale Fe-rich phases still can be seen (as shown in Figs. 7–9), i.e., different number densities and distributions of multi-scale particles. This difference is mainly resulted from the positive effect of Ni micro-alloying on the microstructure in both the as-cast and homogenization states (as shown in Figs. 3 and 4). With these improvements in the microstructure, the final distribution of multi-scale Fe-rich phases in the #2 alloy even treated by the processing route I is also better than that of #1 alloy treated by the same route. However, some micro-cracks still can be observed in the remained coarse Fe-rich phases in the #2 alloy, certainly the number density of micro-cracks in the #2 alloy is much lower than that of the #1 alloy (as shown in Figs. 7 and 20). This further indicates that an appropriate thermomechanical processing is also greatly important to improve the distribution of Fe-rich phases in the alloys.

In order to improve the distribution of Fe-rich phases, the thermomechanical processing route II was designed and used to control the evolution of Fe-rich phases in the #2 alloy. It can be found that not only the number density of fine Fe-rich phases can be increased in the final cold rolled #2 alloy, but also the micro-cracks remained in the coarse particles can be basically avoided (as shown in Figs. 7 and 20). These improvements directly result in the different distribution characteristics of multi-scale Fe-rich particles, and the different recrystallization behaviors, microstructure and mechanical properties of the alloys as discussed above.

In addition, the synergy of Ni micro-alloying and thermomechanical processing also gives a positive influence on the coordinate deformation of grains in the alloys during the tensile deformation or stamping. Figure 21 shows the experimental and visco-plastic self-consistent (VPSC) predicted r values of the #2 alloys treated by the processing routes I and II. It can be seen that a significant difference in the experimental and VPSC predicted r values appears in the #2 alloy treated by the processing route I, while a slight difference appears in the #2 alloy treated by the optimized processing route II. The difference should be mainly resulted from the microstructure characteristic. All these further indicate that the synergy of Ni micro-alloying and thermomechanical processing is greatly important to improve the phase distribution, microstructure and mechanical properties of Al–Mg–Si–Cu–Zn–Fe–Mn alloys.

5. Conclusions

(1) With the addition of micro-alloying Ni, the Ni-containing Fe-rich phase can be formed, which not only serves as nucleation sites of Mg–Si precipitates (such as, Q phase) during the casting process, but also increases the transformation rate of $\beta \rightarrow \alpha$ during the homogenization treatment, and further enhance the number density of spherical α Fe-rich phases and their uniform distribution level in the alloy matrix.

(2) The formability and bendability of Ni-containing alloy can be both improved to a certain level due to the positive effect of micro-alloying Ni. If increasing the cold rolling deformation between hot rolling and annealing, the distribution of multi-scale Fe-rich phases (<1 μm) can be significantly improved based on the synergy of Ni micro-alloying and thermomechanical processing. And finally, this improvement further results in the great improvements in the microstructure, texture, formability (average $r = 0.688$, $\Delta r = -0.09$) and bendability of the alloy together.

(3) Based on the relationship between microstructure and mechanical properties, the synergy mechanism of Ni micro-alloying and thermomechanical processing on the improved phase distribution, microstructure and mechanical properties of the Al–Mg–Si–Cu–Zn–Fe–Mn alloys was put forward in this paper.

Declaration of Competing Interest

No potential conflict of interest was reported by the authors.

Acknowledges

This work was supported by the National Key Research and Development Program of China (2021YFE010225), the National Natural Science Foundation of China (No. 51871029, No. 51571023 and No. 51301016), Government Guided Program - Intergovernmental Bilateral Innovation Cooperation Project (BZ2019019), the Opening Project of State Key Laboratory for Advanced Metals and Materials (2020-ZD02).

REFERENCES

[1] Javidani M, larouche D. Application of cast Al-Si alloys in internal combustion engine components. Int Mater Rev 2014;59:132–58.
[2] Hirsch J, Al-Samman T. Superior light metals by texture engineering: optimized aluminum and magnesium alloys for automotive applications. Acta Mater 2013;61:818–43.
[3] Ma WY, Wang BY, Fu L, Zhou J, Huang MD. Influence of process parameters on deep drawing of AA6111 aluminum alloy at elevated temperatures. J Cent South Univ 2015;22:1167–74.
[4] Hirsch J. Recent development in aluminium for automotive applications. Trans Nonferrous Metals Soc China 2014;24:1995–2002.
[5] Ma WP, Wang BY, Xiao WC, Yang XM, Kang Y. Spring back analysis of 6016 aluminum alloy sheet in hot V-shape stamping. J Cent South Univ 2019;26:524–35.
[6] Zheng Y, Xiao W, Ge S, Zhao W, Hanada S, Ma C. Effects of Cu content and Cu/Mg ratio on the microstructure and mechanical properties of Al-Si-Cu-Mg alloys. J Alloys Compd 2015;649:291–6.
[7] Kim JH, Marioara CD, Holmestad R, Kobayashi E, Sato T. Effects of Cu and Ag additions on age-hardening behavior during multi-step aging in Al-Mg-Si alloys. Mater Sci Eng A 2013;560:154–62.
[8] Gupta AK, Lloyd DJ, Court SA. Precipitation hardening in Al-Mg-Si alloys with and without excess Si. Mater Sci Eng A 2001;316:11–7.
[9] Yan LZ, Zhang YA, Li XW, Li ZH, Wang F. Effect of Zn addition on microstructure and mechanical properties of an AleMgeSi alloy. Prog Nat Sci: Met Mater Int 2014;24:97–100.
[10] Guo MX, Li GJ, Zhang YD, Sha G, Zhang JS, Zhuang LZ, et al. Influence of Zn on the distribution and composition of heterogeneous solute-rich features in peak aged Al-Mg-Si-Cu alloys. Scripta Mater 2019;159:5–8.
[11] Yuan B, Guo MX, Zhang JS, Zhuang LZ, Lavernia EJ. Influence of treatment pathways on the precipitation behaviors of Al-Mg-Si-Cu-(Zn)-Mn alloys. J Alloys Compd 2019;797:26–38.
[12] Guo MX, Zhang XK, Zhang JS, Zhuang LZ. Effect of Zn addition on the precipitation behaviors of Al–Mg–Si–Cu alloys for automotive applications. J Mater Sci 2016;52:1–15.
[13] Guo MX, Zhang YD, Li GJ, Jin SB, Sha G, Zhang JS, et al. Solute clustering in Al-Mg-Si-Cu-(Zn) alloys during aging. J Alloys Compd 2019;774:347–63.
[14] Ji S, Yang W, Gao F, Watson D, Fan Z. Effect of iron on the microstructure and mechanical property of Al-Mg-Si-Mn and Al-Mg-Si diecast alloys. Mater Sci Eng A 2013;564:130–9.
[15] Gorny A, Manickaraj J, Cai ZH. Evolution of Fe based intermetallic phases in Al–Si hypoeutectic casting alloys: influence of the Si and Fe concentrations, and solidification rate. J Alloys Compd 2013;577:103–24.
[16] Xing H, Guo MX, Wang XF, Zhang Y, Zhang JS, Zhuang LZ. Effect of Fe-rich phase particles with different concentrations on the bendability of Al-Mg-Si-Cu series alloys. Acta Metall Sin 2016;52:271–80.
[17] Castany P, Diologent F, Rossoll A, Despois JF, Bezencon C, Mortensen A. Influence of quench rate and microstructure on bendability of AA6016 aluminum alloys. Mater Sci Eng A 2013;559:558–65.
[18] Muhammad W, Kang JD, Brahme AP, Ali U, Hirsch J, Brinkman HJ, et al. Bendability enhancement of an age-hardenable aluminum alloy: Part I —relationship between microstructure, plastic deformation and fracture. Mater Sci Eng A 2019;753:179–91.
[19] Yang H, Watson D, Wang Y, Ji S. Effect of nickel on the microstructure and mechanical property of die-cast Al–Mg–Si–Mn alloy. J Mater Sci 2014;49:8412–22.
[20] Li GJ, Guo MX, Wang Y, Zheng CH, Zhang JS, Zhuang LZ. Effect of Ni addition on microstructure and mechanical properties of Al–Mg–Si–Cu–Zn alloys with a high Mg/Si ratio. Int J Min Metall Mater 2019;26:740–51.
[21] Engler O, Hirsch J. Texture control by thermomechanical processing of AA6xxx Al–Mg–Si sheet alloys for automotive applications—a review. Mater Sci Eng A 2002;336:249–62.
[22] Liu WC, Li Z, Man CS. Effect of heating rate on the microstructure and texture of continuous cast A A 3105 aluminum alloy. Mater Sci Eng A 2008;478:173–80.
[23] Wang XF, Guo MX, Luo JR, Zhu J, Zhang JS, Zhuang LZ. Effect of intermediate annealing time on microstructure, texture

and mechanical properties of Al-Mg-Si-Cu alloy. Mater Char 2018;142:309–20.
[24] Wang XF, Guo MX, Zhang JS, Zhuang LZ. Effect of Zn addition on the microstructure, texture evolution and mechanical properties of Al-Mg-Si-Cu alloys. Mater Sci Eng A 2016;677:522–33.
[25] Wang XF, Guo MX, Ma CQ, Chen JB, Zhang JS, Zhuang LZ. Effect of particle size distribution on the microstructure, texture, and mechanical properties of Al–Mg–Si–Cu alloy. Int J Miner Metal Mater 2018;25:957–66.
[26] Waqas M, Brahme AP. Bendability enhancement of an age-hardenable aluminum alloy: Part II- multiscale numerical modeling of shear banding and fracture. Mater Sci Eng A 2019;754:161–77.
[27] Ohnuma I, Shimenouchi S, Omori T, Ishida K, Kainuma R. Experimental determination and thermodynamic evaluation of low-temperature phase equilibria in the Fe–Ni binary system. Calphad 2019;67:101677.
[28] H Hu X, Jain M, Wu PD. A macro–micro-multi-level modeling scheme to study the effect of particle distribution on wrap-bendability of AA5754 sheet alloys. 210. 2019. p. 1232–42.
[29] Bayat N, Carlberg T, Cieslar M. In-situ study of phase transformations during homogenization of 6060 and 6063 Al alloys. J Phys Chem Solid 2019;130:165–71.
[30] Bayat N, Carlberg T, Cieslar M. In-situ study of phase transformations during homogenization of 6005 and 6082 Al alloys. J Alloys Compd 2017;725:504–9.
[31] Kuijpers NN, Nbsp C. Model of the -AlFeSi to -Al(FeMn)Si transformation in Al–Mg–Si alloys. Mater Trans 2003;44:1448–56.
[32] Alexander DTL, Greer AL. Solid-state intermetallic phase transformations in 3XXX aluminium alloys. Acta Mater 2002;50:2571–83.
[33] Kuijpers NCW, Vermolen FJ, Vuik K, Zwaag SVD. A model of the β-AlFeSi to α-Al(FeMn)Si transformation in Al-Mg-Si alloys. Mater Trans 2003;44:1448–56.
[34] Cao LY, Guo MX, Cui H, Cai YH, Zhang JS. Study on the kinetics of phase transformation β → α in the homogeneous heat treatment of Al-Mg-Si series alloys. Acta Metall Sin 2013;49:428–34.
[35] Qian XM, Parson XN, Chen XG. Effect of homogenization treatment and microalloying with Mn on the microstructure and hot workability of AA6060 aluminum alloys. J Mater Eng Perform 2019;28:4531–42.
[36] Lücke K, Engler O. Effects of particles on development of microstructure and texture during rolling and recrystallisation in fcc alloys. Mater Sci Technol 1990;6:1113–30.
[37] Engler O, Kong XW, Yang P. Influence of particle stimulated nucleation on the recrystallization textures in cold deformed Al-alloys part I—experimental observations. Scripta Mater 1997;37:1665–74.
[38] Humphreys FJ, Hatherly M. Recrystallization and related annealing phenomena. Elsevier; 1995.
[39] Bennett TA, Petrov RH, Kestens LAI. Effect of particles on texture banding in an aluminium alloy. Scripta Mater 2010;62:78–81.
[40] Kuijpers NCW, Vermolen FJ, Vuik C. The dependence of the β-AlFeSi to α-Al(FeMn)Si transformation kinetics in Al–Mg–Si alloys on the alloying elements. Mater Sci Eng A 2005;394:9–19.
[41] Lodgaard L. N Ryum, Precipitation of dispersions containing Mn and/or Cr in Al–Mg–Si alloys. Mater Sci Eng 2000;283:144–52.
[42] Liu SQ. Dispersoid formation and recrystallization behavior in an Al-Mg-Si-Mn alloy. J Mater Sci Technol 2010;26:237–43.